Article

Tolerance Factor Control of Uniaxial Negative Thermal Expansion in a Layered Perovskite

Chris Ablitt, Harriet McCay, Sarah Craddock, Lauren Cooper, Emily Reynolds, Arash A. Mostofi, Nicholas C. Bristowe, Claire A. Murray, and Mark S. Senn

Chem. Mater., **Just Accepted Manuscript** • DOI: 10.1021/acs.chemmater.9b04512 • Publication Date (Web): 16 Dec 2019

Tolerance Factor Control of Uniaxial Negative Thermal Expansion in a Layered Perovskite

Chris Ablitt,[†,‡] Harriet McCay,[¶] Sarah Craddock,[¶] Lauren Cooper,[‡] Emily Reynolds,[¶] Arash A. Mostofi,[†,§] Nicholas C. Bristowe,[†,‖] Claire A. Murray,[⊥] and Mark S. Senn[*,¶,‡]

†*Department of Materials and the Thomas Young Centre, Imperial College London, London, SW7 2AZ, U.K.*

‡*Department of Chemistry, University of Warwick, Gibbet Hill, Coventry, CV4 7AL, U.K.*

¶*Department of Chemistry, University of Oxford, South Parks Road, Oxford, OX1 3QR, U.K.*

§*Department of Physics, Imperial College London, London, SW7 2AZ, U.K.*

‖*School of Physical Sciences, University of Kent, Canterbury, CT2 7NH, U.K.*

⊥*Diamond Light Source, Harwell Campus, Oxfordshire, OX11 0DE, U.K.*

E-mail: m.senn@warwick.ac.uk

Abstract

By tuning the tolerance factor, t, of the Ruddlesden–Popper oxide Ca_2MnO_4 through isovalent substitutions, we show that the uniaxial coefficient of linear thermal expansion (CLTE) of these systems can be systematically changed through large negative to positive values. High-resolution X-ray diffraction measurements show that the magnitude of uniaxial negative thermal expansion (NTE) increases as t decreases across the stability window of the NTE phase. Transitions to phases with positive thermal expansion (PTE) are found to occur at both the high-t and low-t limits of stability. First-principles calculations demonstrate that reducing t enhances the contribution to thermal expansion from the lowest frequency phonons, which

have the character of octahedral tilts and have negative mode Grüneisen parameter components along the NTE axis. By tuning t to the lower edge of the NTE phase stability window, we are hence able to maximise the amplitudes of these vibrations and thereby maximise NTE with a CLTE of -8.1 ppm/K at 125 K. We also illustrate, at the other end of the phase diagram, that an enhancement in compliance of these materials associated with the rotational instability provides another mechanism by which NTE could be yet further enhanced in this and related systems.

Negative thermal expansion (NTE) is the rare phenomenon whereby a material contracts with an increase in temperature. In ceramics, NTE has been found to occur due to several different mechanisms; electronic,[1,2] magnetic[3–5] and vibrational[6,7] in origin. As such, many studies on NTE systems focus on deducing the origin of NTE.[8–10] However, there have also been attempts to investigate methods of controlling NTE, for example by including guest species[11,12] or varying composition.[13–17] The means to tune the magnitude of thermal expansion would be especially useful for device applications: both to match the coefficient of linear thermal expansion (CLTE) between components (preventing the build up of thermal stresses) or to develop materials with near zero thermal expansion (ZTE).[1] The desire to control thermal expansion is paradigmatic of a wider trend in the field of functional oxides to develop materials with tunable properties. However, for the most part, attempts to date have led only to a suppression of the magnitude and/or temperature window of NTE.

Ruddlesden–Popper (RP) oxides are layered perovskites with general formula $A_{n+1}B_nO_{3n+1}$ whose structures consist of blocks of n BO_6 octahedra separated by a single AO rock salt layer (see examples of RP1, i.e. $n = 1$, phases in Figure 1). Certain compounds of RP1 (Ca_2MnO_4,[18,19] Sr_2RhO_4,[20,21] Sr_2IrO_4[22] and Ca_2GeO_4[23]) and RP2 ($Ca_3Mn_2O_7$[24]) oxides exhibit uniaxial NTE (along their layering axis only) over a particularly wide temperature range, often exceeding 1000 K. In all of these cases the NTE is unique to a particular phase, with frozen-in *rotations* of octahedra about the layering axis but no frozen *tilts* about in-plane axes – the well-defined layering axis in RP structures means that it is customary to distinguish between *rotations* and *tilts* in this man-

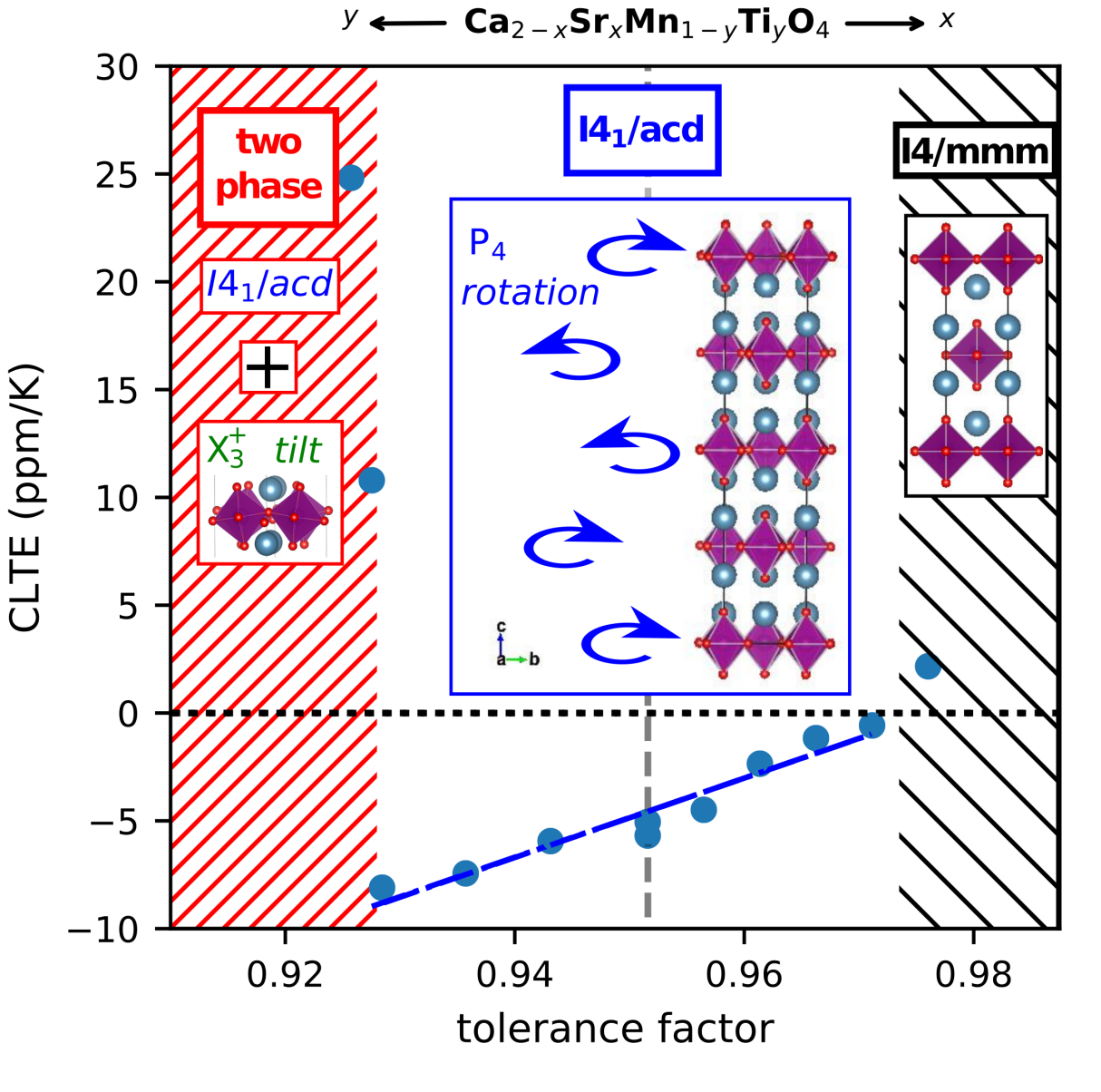

Figure 1: Coefficient of linear thermal expansion (CLTE) along the layering axis as a function of tolerance factor, t, computed by numerical differentiation at 125 K of c lattice parameters extracted using high-resolution X-ray diffraction. Qualitative phase diagram at this temperature also shown with frozen octahedral distortions to the $I4/mmm$ aristotype illustrated and labelled according to the irreducible representation (irrep) they transform as. The precise nature of the secondary phase in the low-t two-phase samples could not be established, yet there is evidence it has a frozen octahedral tilt (with character of the X_3^+ irrep) Vertical grey dashed line indicates pure Ca_2MnO_4.

ner. Transformation with temperature to a higher[20–22] or lower[24] symmetry phase corresponds to a switch from negative to positive thermal expansion (PTE). In a previous work, we found that uniaxial NTE in RP1 Ca_2GeO_4 is driven by both (i) active octahedral tilt vibrations and (ii) a high elastic compliance,[25] caused by an atomic *corkscrew mechanism* in RP phases with a frozen octahedral rotation.[26] The Goldschmidt tolerance factor, t, is a metric that has been linked with the propensity for BO_6 octahedra to tilt in ABO_3 perovskites. Chemical substitution has been used to control various RP properties in several experimental and computational studies.[27–31] Increasing the proportion of the Sr on the Ca site – thus increasing t – in ($n = 2$) $Ca_{3-x}Sr_xMn_2O_7$ has previously been found to reduce the magnitude of uniaxial NTE, with a switch to PTE above $x = 1.5$ correlating with a transformation to the undistorted parent phase.[32] A more recent computational study of ours predicted that NTE should be greatest in the RP rotation phases with the lowest n.[33]

In this work, we realise this prediction by using chemical substitution to engineer an RP1 system that spans the full low-temperature stability range of the NTE phase. We form two solid solutions based around Ca_2MnO_4: the first by substituting Sr onto the Ca-site and the second by replacing Mn with Ti. Introducing these larger cations onto Ca or Mn sites allows us to both increase and decrease the tolerance factor, respectively. Finding that the magnitude of uniaxial NTE at 125 K is greatest just before the transition to a region of two-phase coexistence, we reason that we have maximised uniaxial NTE with respect to composition for this system. We go on to use the results of first-principles simulations to demonstrate the mechanism through which chemical control acts to tune the CLTE. We show that the frequency of octahedral tilt vibrations drop as t is reduced, suggesting that these NTE-driving modes more greatly impact the overall lattice dynamics. The compliance to cooperative strains associated with uniaxial NTE also drops as t is lowered. However, a peak in this compliance predicted at values of t just below the transition to the undistorted parent phase (in which the frozen octahedral rotation is lost) is consistent with a large enhancement in experimental uniaxial NTE observed in $Ca_2Mn_{0.4}Ti_{0.6}O_4$ as this transition is approached with temperature.

Experimental

Polycrystalline samples of the first solid solution, $Ca_{2-x}Sr_xMnO_4$ ($0 \leq x \leq 1$) were prepared via conventional solid state synthesis methods. $Ca_2Mn_{1-y}Ti_yO_4$ has recently been reported as being prepared by this method,[34] yet in practice we found it hard to achieve phase pure sample, yielding high proportions of RP2 and ABO_3 perovskite impurities. For $y = 0 - 0.7$ 1.8g $\approx$ 9 mmol were instead prepared using a sol-gel method in which stoichiometric amounts of $Ca(NO_3)_2{\cdot}4H_2O$ and $Mn(NO_3)_2{\cdot}4H_2O$ were dissolved in a HNO_3 solution (15 ml, 30 %) with constant stirring. A second solution made by adding stoichiometric amounts of $Ti(OC_4H_9)_4$ to a solution of 100 ml ethanol with 10 ml glacial acetic acid, which was then added slowly to the first solution and left stirring until a transparent solution was obtained. While stirring, additional citric acid was added. The mixture was then heated up to approx 300 °C until the solution formed a gel, and finally a powder. The powder was pressed into pellets and sintered at 500°C in air for 12 hours to yield the precursor powder. This powder was ground and fired at 1250°C under flowing oxygen three times for 12 hour periods with intermediate regrinding.

Results and discussion

Figure 1 shows the phase diagram at 125 K as a function of tolerance factor[1] for both solid solutions as established from Rietveld fits to the weak (super)structure peaks. Example XRD diffraction patterns at 300 K may be seen for $x = 1.0, 0$ and $y = 0.625, 0.7$ samples in Figure 2. Compositions with low and intermediate values of x ($x = 0.0, 0.2, 0.4, 0.6 \& 0.8$) and y ($y = 0.0, 0.225, 0.425, 0.625$) crystallise in the space group $I4_1/acd$ over the full temperature range studied (100–500 K for $Ca_{2-x}Sr_xMnO_4$ and 85–300 K for most $Ca_2Mn_{1-y}Ti_yO_4$ compounds). This phase is a distortion of the aristotype $I4/mmm$ with an octahedral rotation frozen in about the c-axis (the layering axis) that is anti-phase between adjacent $I4/mmm$ cells (see Figure 1). Such a rotation has the propagation vector $k = \left[\frac{1}{2}\,\frac{1}{2}\,\frac{1}{2}\right]$ and transforms as the irreducible representation P_4 with respect to the

parent symmetry $I4/mmm$ (setting with Mn at $(0,0,0)$).

Although the superstructure peaks are hard to resolve from the background at higher values of x, the inset of Figure 2 shows the absence of any weak superstructure peaks at $x = 1$ which are characteristic of the $I4_1/acd$ phase. There is also a discontinuity in the c/a ratios between $x = 0.8$ and 1.0 (Figure S1 in the SI). This indicates that the $x = 1$ compound adopts the parent $I4/mmm$ phase. At the lower end of the t-range, the two highest y samples ($y = 0.65, 0.7$) are well-described by the $I4_1/acd$ fit at 300 K. However, at 100 K, although many of the super structure peaks were fit well by the $I4_1/acd$ model, substantial asymmetric peak broadening across the entire pattern suggests a secondary RP phase to be present with symmetry lower than that of the parent structure. Furthermore, weak additional reflections at $2\theta = 21.5^\circ$ (inset bottom panel Figure 2) imply that the coexisting phase has frozen octahedral tilts with X_3^+ character, which is likely to have *Pbca* symmetry similar to Ca_2RuO_4.[36] This two phase mixture thus indicates a second boundary to the low temperature pure $I4_1/acd$ stability region, however, the precise space group assignment is beyond the scope of the current study.

We performed temperature-dependent XRD studies on the high resolution powder diffractometer I11 at Diamond Light Source with $\lambda \approx 0.826$ Å to determine lattice parameters and thermal expansion coefficients. All samples display PTE with respect to the volume and the a lattice parameter (see Figure S2). From the CLTEs for all compounds presented in Figure 1, we see that all samples that index as purely $I4_1/acd$ (those with $0.928 < t < 0.974$) exhibit NTE of the c axis at 125 K. The CLTE – obtained from linear interpolation of c measurements over the range [115, 135] K – varies approximately linearly with tolerance factor, decreasing as t increases. Plots of axial strain (relative to the 100 K measurement) for $x = y = 0$ and $y = 0.625$ samples in Figure 2 demonstrate that NTE persists at all temperatures. As the temperature increases, the magnitude of uniaxial NTE decreases over the temperature range shown. The transformation to the parent $I4/mmm$ phase in the high-t sample ($x = 1$) corresponds with a switch to PTE of the c axis at all temperatures. Similarly, at low t, the two-phase samples ($y = 0.65, 0.7$) both display large PTE

[1]Shannon radii[35] have been used to compute all A_2BO_4 tolerance factors, t, based on the mean radii of IX-coordinate A^{2+} and VI-coordinate B^{4+} cations.

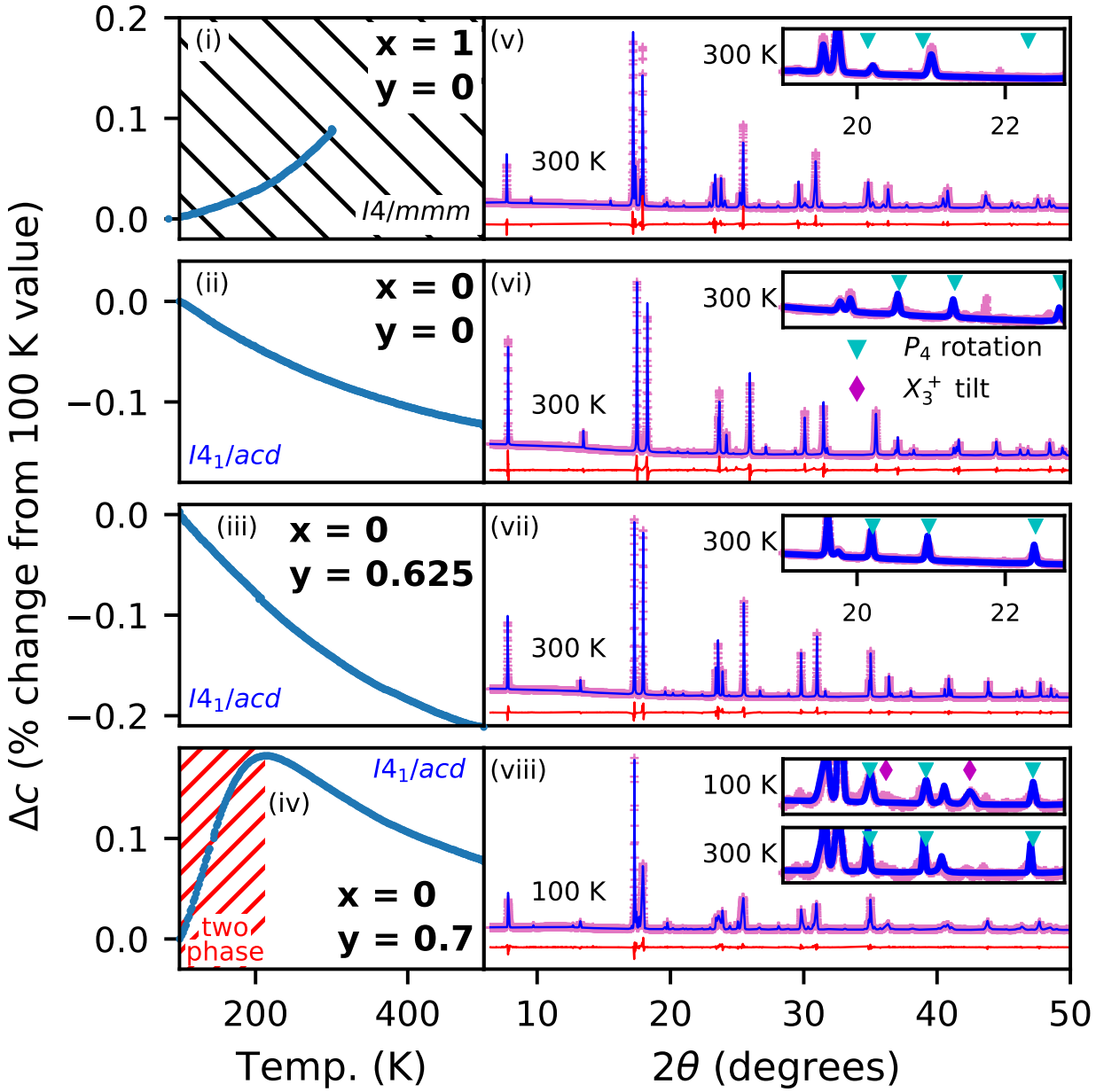

Figure 2: (i)–(iv) Left-hand plots show axial strain relative to c measured at 100 K, with hatching indicating temperature regimes of non-$I4_1/acd$ phases. (v)–(viii) Right-hand plots show Rietveld refinement fits to the XRD data ($\lambda \approx 0.826$ Å) of polycrystalline $Ca_{2-x}Sr_xMnO_4$ and $Ca_2Mn_{1-y}Ti_yO_4$. The insets show a region where multiple superstructure peaks are present in the $I4_1/acd$ phase but absent in $I4/mmm$ (cyan triangles). Superstructure peaks absent in (v) $x = 1$ evidence $I4/mmm$ symmetry. Purple diamonds evidence additional peaks characteristic of the X_3^+ irrep in (viii) $y = 0.7$ (100 K). A small peak due to a CaO impurity (between 0.2 and 2 %) is present at 19.75° in all refinements. Ruddlesden–Popper $n = 2$ phase forms an impurity 19 % by weight in (v) $x = 1$ and 10 % by weight in (viii) $y = 0.7$.

along c at 125 K, even though uniaxial NTE is observed in these compounds above their transitions to single-phase $I4_1/acd$ at around 160 K and 215 K, respectively. We thus demonstrate that uniaxial NTE is unique to RP phases with frozen octahedral rotations and that the magnitude of NTE may be controlled by changing t. By tuning the chemistry so as to minimise the tolerance factor whilst remaining in the single-phase $I4_1/acd$ region, we have been able to maximise NTE at 125 K in the $y = 0.625$ compound, with a CLTE value of -8.1 ppm/K.

To investigate the origin of this dependence of the CLTE upon tolerance factor, we performed first-principles simulations, modelling changes in composition using the virtual crystal approximation (VCA). It was not possible to explicitly simulate the $Ca_2Mn_{1-y}Ti_yO_4$ series using the VCA within a 56-atom $I4_1/acd$ cell, since the Mn pseudopotential had 15 valence electrons and the Ti pseudopotential had 12, and therefore no ratio of Mn and Ti could be found that left an integer number of valence electrons per ion. As a result, we simulated changes in B-site cation radius by substituting larger, yet isovalent, Tc onto the Mn site, covering the full range of t realised in experiment. Additionally, we also simulated pure Ca_2TiO_4. All simulations used CASTEP v7.0.3[37] to perform density functional theory (DFT), employing the PBEsol functional[38] to model exchange and correlation. We used norm-conserving pseudopotentials (details may be found in Table S1), with a 1400 eV plane-wave cut-off energy. A grid of k-points was employed with equivalent density in reciprocal space to a $7 \times 7 \times 2$ grid in the 14-atom $I4/mmm$ Ca_2MnO_4 cell. For structural relaxations, forces were converged to 0.1 meV/Å and stresses to 10 MPa. Each Mn^{4+}/Tc^{4+} ion was given an initial spin configuration of $3\mu_B$ (only co-linear spins were considered) with in-plane checkerboard anti-ferromagnetic ordering (this configuration was found to be lowest in energy for $I4_1/acd$ Ca_2MnO_4). All $Ca_{2-x}Sr_xMn_{1-y'}Tc_{y'}O_4$ compositions were found to be insulators (with at least a small electronic band gap) and therefore no additional Hubbard parameter was employed.

The bottom panel of Figure 3 compares the energy of the $I4_1/acd$ NTE phase and an orthorhombic $Pbca$ phase[2] (with frozen X_2^+ rotations and X_3^+ tilts) to that of the $I4/mmm$ aristotype as a function of tolerance factor. The lowest energy phase for each composition is denoted as the ground state. The $I4/mmm \rightarrow I4_1/acd \rightarrow Pbca$ sequence of predicted ground-state phases with

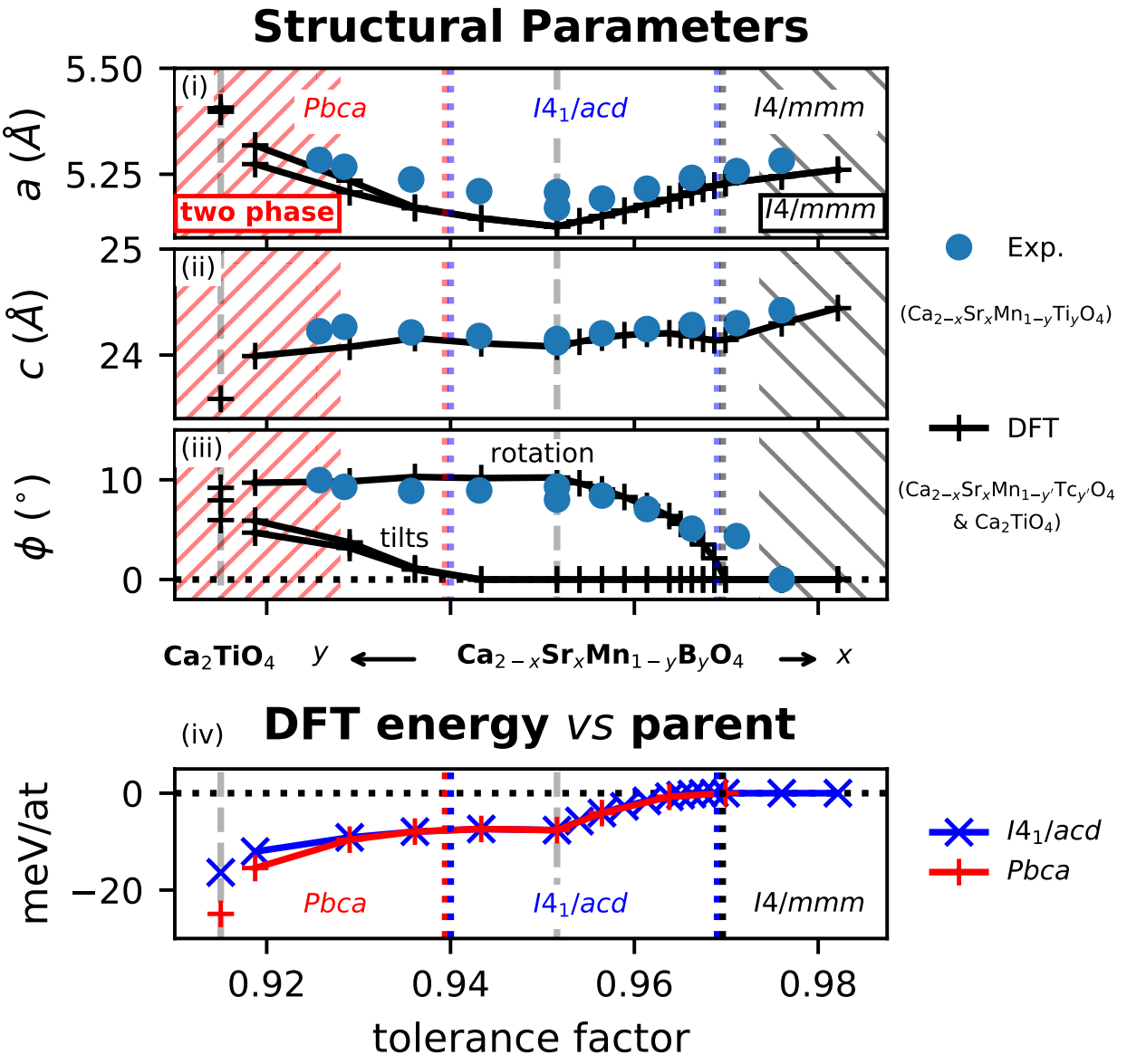

Figure 3: (i) a (& b) and (ii) c lattice parameters and (iii) BO_6 octahedral rotation/tilt angles (about ideal B–O bond axes) comparing 100 K experimental measurements (refined as $I4_1/acd$) with the simulated ground-state structure. (iv) Energies of relaxed phases compared to the $I4/mmm$ parent (in meV/atom). Hashed regions denote non-$I4_1/acd$ experimental compounds and pairs of vertical dashed lines represent boundaries between different simulated ground-state phases. Vertical grey dashed lines indicate pure Ca_2MnO_4 or Ca_2TiO_4.

reducing t (boundaries shown by vertical dashed lines) qualitatively agrees with those of the 100 K experiment (non-$I4_1/acd$ phases shown hatched) in the upper three panels of Figure 3, although the $I4_1/acd$ stability window is predicted to be narrower in simulations. Structural parameters (lattice parameters and octahedral rotation angle) also agree very closely between the relaxed ground state and low temperature measurements (treating all compounds as pure $I4_1/acd$). We also simulated the $Ca_{2-x}Sr_xGe_{1-y''}Sn_{y''}O_4$ series, which previously we had used as proxy for the manganate system[25,32,33] and found qualitatively identical behaviour of this system with changing t (Figures S3–S5 in the SI).

We have previously shown that uniaxial NTE in ($n = 1$) Ca_2GeO_4 arises from two ingredients: (i) low-frequency octahedral *tilt* modes that drive axial NTE and in-plane PTE and (ii) highly anisotropic elastic compliance (which may be explained by an atomistic *corkscrew mechanism*[26]) that causes the in-plane expansion to couple to uniaxial NTE.[25] To decouple which of these effects is most strongly influenced by changes in composition, Figure 4 compares the Γ-point phonon frequencies and the eigenvalues of the elastic compliance matrix against t. Since the $I4_1/acd$ stability window is wider in experiment, all simulations in Figure 4 were performed on the $I4_1/acd$ phase (unless this relaxed to the $I4/mmm$ parent) even if *Pbca* is the ground-state at low t. For such compositions the compliance and frequency curves are dashed.

Within the $I4_1/acd$ NTE phase, octahedral tilt modes (whose eigenvectors have character of the X_3^+, X_4^+ or P_5 parent irreps - coloured green in Figure 4) generally soften as t is reduced, indicating that the population of these modes increase and they contribute more strongly to the overall lattice dynamics. This echoes past results in $Ca_{3-x}Sr_xMn_2O_7$.[32] Simulations on non-magnetic $Ca_{2-x}Sr_xGe_{1-y''}Sn_{y''}O_4$ (see SI) show that the magnitude of the anisotropic Grüneisen parameters (a measure of how much each phonon contributes to the total thermal expansion) of these lowest frequency tilts become very large as these modes soften. In both systems, the softest tilt frequency is lowest and the anisotropic Grüneisen parameter is greatest just before the boundary at which the

[2]Freezing X_3^+ tilts into $I4_1/acd$ also creates a *Pbca* ($P_4 \oplus X_3^+$) phase. However, this was found in simulations on Ca_2TiO_4 and Ca_2GeO_4 to be higher in energy and has double the unitcell volume compared to *Pbca* ($X_2^+ \oplus X_3^+$). To the best of our knowledge, it is also not found as the experimental low-temperature phase for any RP1 compound, unlike *Pbca* ($X_2^+ \oplus X_3^+$).

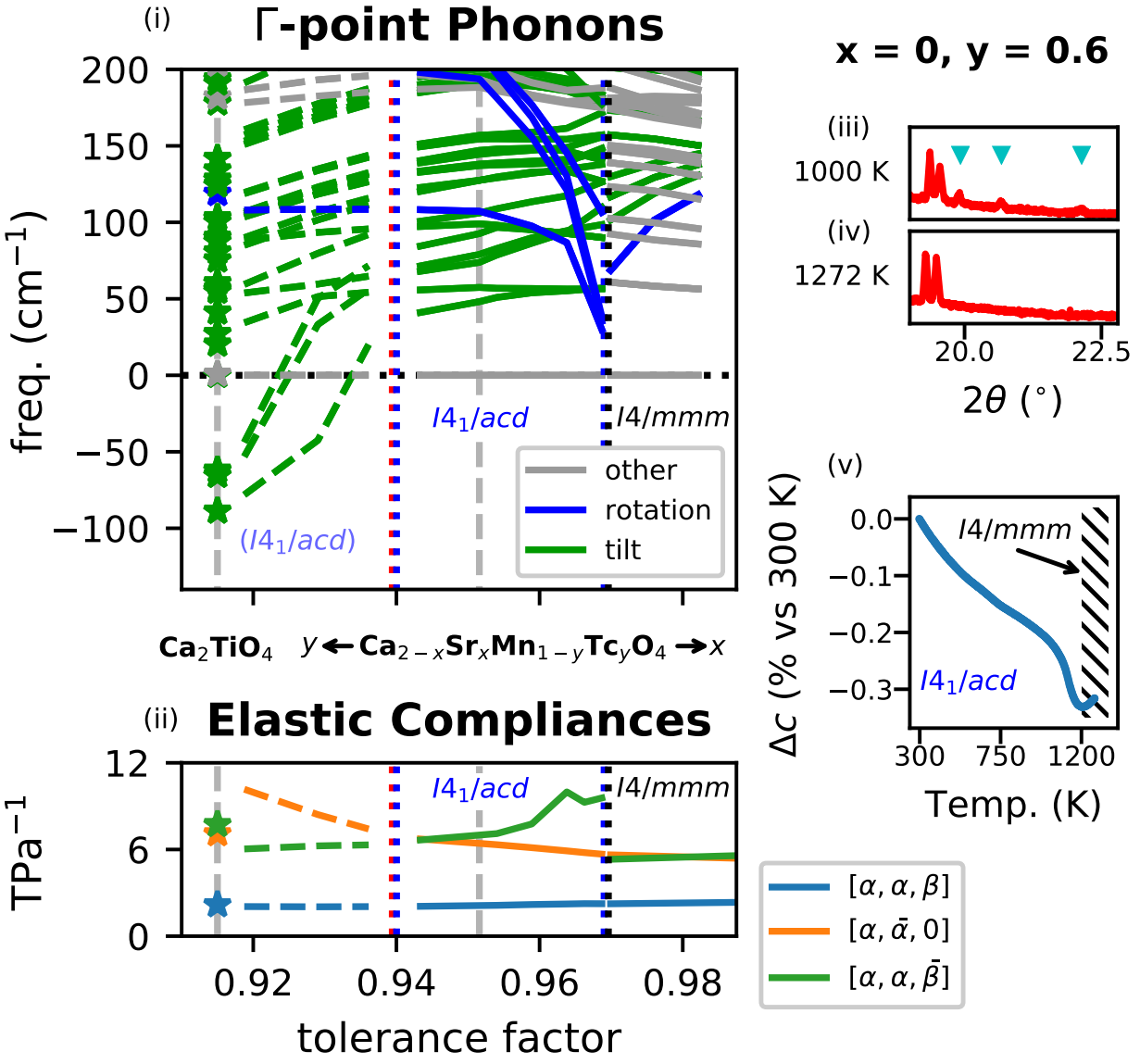

Figure 4: (i) Phonons computed at the Γ-point of a 56-atom $I4_1/acd$ cell ($\sqrt{2}\times\sqrt{2}\times 2$ supercell of $I4/mmm$). Octahedral *tilts* (having eigenvectors with the character of X_3^+, X_4^+ or P_5 irreps for the $I4/mmm$ cell) are coloured green and *rotations* (X_2^+ or P_4 irreps) are coloured blue with all other modes grey. (ii) Eigenvalues to the elastic compliance matrix coloured according to their associated eigenvector. In both plots, $I4_1/acd$ phases are simulated at low t, even for t where the ground state was found to be *Pbca*. Pairs of vertical dashed lines represent boundaries between different simulated ground-state phases and vertical grey dashed lines indicate pure Ca_2MnO_4 or Ca_2TiO_4. High-temperature diffraction patterns at (iii) 1000 K and (iv) 1272 K showing transition from $I4_1/acd$ NTE phase (peaks indicated by cyan triangles) to $I4/mmm$ parent in $Ca_2Mn_{0.4}Ti_{0.6}O_4$. (v) Change in c measured using high-resolution XRD relative to 300 K value (black dashed region indicates $I4/mmm$).

Pbca phase becomes the ground-state. At this boundary, the softest tilt frequency becomes imaginary (shown as negative) and the system becomes most compliant to orthorhombic distortions. We may hence conclude that the magnitude of uniaxial NTE is controlled by the proximity to this low-t phase boundary.

In contrast with the octahedral tilt modes, the eigenvalue associated with the elastic compliance eigenvector relevant for NTE, that couples in-plane expansions to out-of-plane contractions (also green in Figure 4) is less sensitive to changes in t and even shows the opposite trend to that expected from the experimental data, decreasing as t is reduced. There is also a large increase in the value of this eigenvalue approaching the $I4_1/acd \rightarrow I4/mmm$ phase boundary. In practice, experimentally we do not observe an enhancement in uniaxial NTE approaching the $I4_1/acd \rightarrow I4/mmm$ phase boundary in Figure 1. Figure 3 shows that we also do not observe experimentally a dip in c approaching this boundary or very low values of the rotation angle, θ, both predicted by DFT. This may be due to a more coarse sampling of compositions. However, high-temperature measurements performed on the $y = 0.6$ sample (Figure 4) evidence a surge in uniaxial NTE, which reaches a maximum (negative) CLTE of -11.5 ppm/K at 1130 K, just below a switch in the sign of thermal expansion around 1205 K (see Figure S7). This NTE $\rightarrow$ PTE switch is accompanied by the loss of superstructure peaks characteristic of the $I4_1/acd$ phase (also shown in Figure 4) indicating that this phase boundary is crossed in temperature. This is consistent with previous high-temperature measurements on Sr_2IrO_4 that show the same phase transition on warming[22] and in which a similar enhancement of uniaxial NTE can be observed. The anomalous behaviour seen in the compliance eigenvalue is expected with increasing temperature (or tolerance factor) across second-order co-elastic transitions,[39] which we demonstrate for our system using a Landau expansion in the SI. In this sense, we have shown tolerance factor to be analogous to temperature in this study, not only because we capture the co-elastic behaviour in proximity of this high-temperature/high-tolerance factor phase transition. In addition, the steadily decreasing magnitude of the measured CLTE as temperature increases up to around 800 K implies a reduced thermodynamic driving force for NTE. This reduction is concurrent with the hardening of octahedral tilt modes with increasing

t in simulations. Hence, by considering both the soft mode energy and elastic compliance, our computational experiment explains the enhancement of NTE at both phase boundaries whether they be crossed in composition or temperature.

In this study we have maximised NTE by selecting a Ruddlesden–Popper system with the lowest layer thickness, $n = 1$ (which had previously been shown to be optimal for compliance[33]) and then tuning tolerance factor to the low-t edge of NTE phase stability window, where the CLTE is most negative. We were thus able to synthesise a compound with a CLTE of -8.1 ppm/K at 125 K, which represents record low-temperature uniaxial NTE in a RP rotation phase (compared to -7.6 ppm/K in Ca_2GeO_4 at 150 K[23]). We also demonstrated that by changing composition, the CLTE may be tuned smoothly through to positive values. Octahedral tilt frequencies are most favourable for NTE at the lower t (or lower temperature) stability boundary of the NTE phase, whereas elastic compliance is greatest at the high-t boundary. If a system could be engineered that was simultaneously *close* to both phase transitions and yet where the NTE phase was stable over a wide temperature range, then this would provide a further route to optimise uniaxial NTE. Whilst these requirements may appear to oppose one another, engineering composite materials with different CLTEs may make it possible to operate close to such phase instabilities over a sustained temperature range. Controlling lattice dynamics in this manner may not only serve for the design of material with unusual thermal expansion properties, but might also be used as a means for tuning ionic and thermal conductivity as well as dielectric properties in the broader family of Ruddlesden–Popper materials.

Associated content

Supporting information

The SI is available free of charge via the internet at http://pubs.acs.org. It contains the SI document (referenced within the text) alongside crystallographic information files of structures at 100 K and 300 K and lattice parameter versus temperature data for all compounds.

Simulation output files can be accessed on figshare at DOI:10.6084/m9.figshare/10110953 and used under the Creative Commons Attribution license.

Acknowledgements

The beamtime used in this paper was through the Diamond Light Source Block Allocation Group award Oxford/Warwick Solid State Chemistry BAG to probe composition-structure-property relationships in solids (EE18786). MSS acknowledges the Royal Society for a fellowship. CA was supported through a studentship in the Centre for Doctoral Training on Theory and Simulation of Materials at Imperial College London funded by the EPSRC (EP/L015579/1). Calculations were performed on the Imperial College London high-performance computing facility. This work was supported by the Thomas Young Centre under grant TYC-101. We are grateful to the UK Materials and Molecular Modelling Hub for computational resources, which is partially funded by EPSRC (EP/P020194/1). This project has received funding from the European Horizon 2020 research and innovation program under the Marie-Skłodowska-Curie grant agreement 641887 (DEFNET).

References

(1) Chen, J.; Hu, L.; Deng, J.; Xing, X. Negative thermal expansion in functional materials: controllable thermal expansion by chemical modifications. *Chem. Soc. Rev.* **2015**, *44*, 3522–3567.

(2) Azuma, M.; Chen, W. T.; Seki, H.; Czapski, M.; Olga, S.; Olga, K.; Mizumaki, M.; Watanuki, T.; Ishimatsu, N.; Kawamura, M.; Ishiwata, S.; Tucker, M. G.; Shimakawa, Y.; Attfield, J. P. Colossal negative thermal expansion in BiNiO3 induced by intermetallic charge transfer. *Nat. Commin.* **2011**, *2*, 347.

(3) van Schilfgaarde, M.; Abrikosov, I.; Johansson, B. Origin of the Invar effect in iron–nickel alloys. *Nature* **1999**, *400*, 46.

(4) Andreev, A.; de Boer, F.; Jacobs, T.; Buschow, K. Thermal expansion anomalies and spontaneous magnetostriction in R2Fe17Cx intermetallic compounds. *Physica B* **1991**, *175*, 361 – 369.

(5) Takenaka, K. Negative thermal expansion materials: technological key for control of thermal expansion. *Sci. Technol. Adv. Mater.* **2012**, *13*, 013001.

(6) Barrera, G. D.; Bruno, J. A. O.; Barron, T. H. K.; Allan, N. L. TOPICAL REVIEW: Negative thermal expansion. *J. Phys. Condens. Matter* **2005**, *17*, 217–252.

(7) Dove, M. T.; Fang, H. Negative thermal expansion and associated anomalous physical properties: review of the lattice dynamics theore tical foundation. *Rep. Prog. Phys.* **2016**, *79*, 066503.

(8) Mittal, R.; Gupta, M.; Chaplot, S. Phonons and anomalous thermal expansion behaviour in crystalline solids. *Prog. Mater. Sci.* **2018**, *92*, 360 – 445.

(9) Liu, Z.; Gao, Q.; Chen, J.; Deng, J.; Lin, K.; Xing, X. Negative thermal expansion in molecular materials. *Chem. Commun.* **2018**, *54*, 5164–5176.

(10) Attfield, J. P. Mechanisms and Materials for NTE. *Front. Chem.* **2018**, *6*, 371.

(11) Chen, J. et al. Tunable thermal expansion in framework materials through redox intercalation. *Nat. Commun.* **2017**, *8*, 14441.

(12) Gao, Q.; Chen, J.; Sun, Q.; Chang, D.; Huang, Q.; Wu, H.; Sanson, A.; Milazzo, R.; Zhu, H.; Li, Q.; Liu, Z.; Deng, J.; Xing, X. Switching Between Giant Positive and Negative Thermal Expansions of a YFe(CN)6-based Prussian Blue Analogue Induced by Guest Species. *Angew. Chemie - Int. Ed.* **2017**, *56*, 9023–9028.

(13) Chen, J.; Wang, F.; Huang, Q.; Hu, L.; Song, X.; Deng, J.; Yu, R.; Xing, X. Effectively control negative thermal expansion of single-phase ferroelectrics of PbTiO 3-(Bi, La) FeO 3 over a giant range. *Sci. Rep.* **2013**, *3*, 2458.

(14) Takenaka, K.; Takagi, H. Giant negative thermal expansion in Ge-doped anti-perovskite manganese nitrides. *Appl. Phys. Lett.* **2005**, *87*, 261902.

(15) Hu, L.; Chen, J.; Fan, L.; Ren, Y.; Rong, Y.; Pan, Z.; Deng, J.; Yu, R.; Xing, X. Zero Thermal Expansion and Ferromagnetism in Cubic Sc1–xMxF3 (M = Ga, Fe) over a Wide Temperature Range. *J. Am. Chem. Soc.* **2014**, *136*, 13566–13569, PMID: 25233253.

(16) Nakajima, N.; Yamamura, Y.; Tsuji, T. Synthesis and physical properties of negative thermal expansion materials Zr1xMxW2O8y (M=Sc, In, Y) substituted for Zr(IV) sites by M(III) ions. *Solid State Commun.* **2003**, *128*, 193 – 196.

(17) Tallentire, S. E.; Child, F.; Fall, I.; Vella-Zarb, L.; Evans, I. R.; Tucker, M. G.; Keen, D. A.; Wilson, C.; Evans, J. S. O. Systematic and Controllable Negative, Zero, and Positive Thermal Expansion in Cubic Zr1–xSnxMo2O8. *J. Am. Chem. Soc.* **2013**, *135*, 12849–12856, PMID: 23895493.

(18) Takahashi, J.; Kamegashira, N. X-ray structural study of calcium manganese oxide by Rietveld analysis at high temperatures. *MRS Bull.* **1993**, *28*, 565 – 573.

(19) Autret, C.; Martin, C.; Hervieu, M.; Retoux, R.; Raveau, R.; André, G.; Bourée, F. Structural investigation of Ca2MnO4 by neutron powder diffraction and electron microscopy. *J. Solid State Chem.* **2004**, *177*, 2044–2052.

(20) Vogt, T.; Buttrey, D. Temperature Dependent Structural Behavior of Sr_2RhO_4. *J. Solid State Chem.* **1996**, *123*, 186 – 189.

(21) Ranjbar, B.; Kennedy, B. J. Anisotropic thermal expansion in Sr_2RhO_4 - A variable temperature Synchrotron X-ray diffraction study. *Solid State Sci.* **2015**, *49*, 43 – 46.

(22) Ranjbar, B.; Kennedy, B. J. Unusual thermal expansion of Sr2IrO4: A variable temperature synchrotron X-ray diffraction study. *J. Solid State Chem.* **2015**, *232*, 178 – 181.

(23) Chen, W.-T.; Ablitt, C.; Bristowe, N. C.; Mostofi, A. A.; Saito, T.; Shimakawa, Y.; Senn, M. S. Negative thermal expansion in high pressure layered perovskite Ca2GeO4. *Chem. Commun.* **2019**, *55*, 2984–2987.

(24) Senn, M. S.; Bombardi, A.; Murray, C. A.; Vecchini, C.; Scherillo, A.; Lui, X.; Cheong, S. W. Negative Thermal Expansion in Hybrid Improper Ferroelectric Ruddlesden-Popper Perovskites by Symmetry Trapping. *Phys. Rev. Lett.* **2015**, *114*, 035701.

(25) Ablitt, C.; Craddock, S.; Senn, M. S.; Mostofi, A. A.; Bristowe, N. C. The origin of uniaxial negative thermal expansion in layered perovskites. *npj Comp. Mater.* **2017**, *3*, 44.

(26) Ablitt, C.; Senn, M. S.; Bristowe, N. C.; Mostofi, A. A. A corkscrew model for highly coupled anisotropic compliance in Ruddlesden-Popper oxides with frozen octahedral rotations. 2018, arxiv:1810.02697. *arXiv*. https://arxiv.org/abs/1810.02697 (accessed December 12, 2019).

(27) Liu, X. Q.; Wu, J. W.; Shi, X. X.; Zhao, H. J.; Zhou, H. Y.; Qiu, R. H.; Zhang, W. Q.; Chen, X. M. Hybrid improper ferroelectricity in Ruddlesden-Popper Ca3(Ti,Mn)2O7 ceramics. *Applied Physics Letters* **2015**, *106*, 202903.

(28) Huang, F.-T.; Gao, B.; Kim, J.-W.; Luo, X.; Wang, Y.; Chu, M.-W.; Chang, C.-K.; Sheu, H.-S.; Cheong, S.-W. Topological defects at octahedral tilting plethora in bi-layered perovskites. *npj Quantum Materials* **2016**, *1*, 16017.

(29) Liu, B.; Huang, Y. H.; Song, K. X.; Li, L.; Chen, X. M. Structural evolution and microwave dielectric properties in Sr2(Ti1-xSnx)O4 ceramics. *Journal of the European Ceramic Society* **2018**, *38*, 3833 – 3839.

(30) Liu, X. Q.; Chen, B. H.; Lu, J. J.; Hu, Z. Z.; Chen, X. M. Hybrid improper ferroelectricity in B-site substituted Ca3Ti2O7: The role of tolerance factor. *Applied Physics Letters* **2018**, *113*, 242904.

(31) Yoshida, S.; Akamatsu, H.; Tsuji, R.; Hernandez, O.; Padmanabhan, H.; Sen Gupta, A.; Gibbs, A. S.; Mibu, K.; Murai, S.; Rondinelli, J. M.; Gopalan, V.; Tanaka, K.; Fujita, K. Hybrid Improper Ferroelectricity in (Sr,Ca)3Sn2O7 and Beyond: Universal Relationship between Ferroelectric Transition Temperature and Tolerance Factor in n = 2 Ruddlesden–Popper Phases. *J. Am. Chem. Soc.* **2018**, *140*, 15690–15700.

(32) Senn, M. S.; Murray, C. A.; Luo, X.; Wang, L.; Huang, F.-T.; Cheong, S.-W.; Bombardi, A.; Ablitt, C.; Mostofi, A. A.; Bristowe, N. C. Symmetry Switching of Negative Thermal Expansion by Chemical Control. *J. Am. Chem. Soc.* **2016**, *138*, 5479.

(33) Ablitt, C.; Mostofi, A. A.; Bristowe, N. C.; Senn, M. S. Control of Uniaxial Negative Thermal Expansion in Layered Perovskites by Tuning Layer Thickness. *Front. Chem.* **2018**, *6*, 455.

(34) Oka, R.; Masui, T. Synthesis and characterization of black pigments based on calcium manganese oxides for high near-infrared (NIR) reflectance. *RSC Adv.* **2016**, *6*, 90952–90957.

(35) Shannon, R. D. Revised effective ionic radii and systematic studies of interatomic distances in halides and chalcogenides. *Acta Crystallogr.* **1976**, 751–767.

(36) Braden, M.; André, G.; Nakatsuji, S.; Maeno, Y. Crystal and magnetic structure of Ca2RuO4: Magnetoelastic coupling and the metal-insulator transition *Phys. Rev. B* **1998**, *58*, 847–861.

(37) Clark, S. J.; Segall, M. D.; Pickard, C. J.; Hasnip, P. J.; Probert, M. J.; Refson, K.; Payne, M. First principles methods using CASTEP. *Z. Kristall.* **2005**, *220*, 567–570.

(38) Perdew, J. P.; Ruzsinszky, A.; Csonka, G. I.; Vydrov, O. A.; Scuseria, G. E.; Constantin, L. A.; Zhou, X.; Burke, K. Restoring the Density-Gradient Expansion for Exchange in Solids and Surfaces. *Phys. Rev. Lett.* **2008**, *100*, 136406.

(39) Carpenter, M. A.; Salje, E. K. Elastic anomalies in minerals due to structural phase transitions. *European Journal of Mineralogy* **1998**, 693–812.